JGR Space Physics

RESEARCH ARTICLE
10.1029/2020JA028670

Key Points:
- We study the global structures of flux ropes formed by magnetopause reconnection in cases with different southward IMF clock angles
- When flux ropes enter the cusps, their helical structure collapses, their core field weakens gradually, and their axial length decreases
- IMF clock angle can affect whether and where flux ropes coalescence occurs

Supporting Information:
- Supporting Information S1

Correspondence to:
S. Lu and Q. M. Lu,
slu@igpp.ucla.edu;
qmlu@ustc.edu.cn

Citation:
Guo, J., Lu, S., Lu, Q., Lin, Y., Wang, X., Huang, K., et al. (2021). Structure and coalescence of magnetopause flux ropes and their dependence on IMF clock angle: Three-dimensional global hybrid simulations. *Journal of Geophysical Research: Space Physics*, *126*, e2020JA028670. https://doi.org/10.1029/2020JA028670

Received 9 SEP 2020
Accepted 29 DEC 2020

Structure and Coalescence of Magnetopause Flux Ropes and Their Dependence on IMF Clock Angle: Three-Dimensional Global Hybrid Simulations

Jin Guo[1,2], San Lu[3], Quanming Lu[1,2], Yu Lin[4], Xueyi Wang[4], Kai Huang[1,2], Rongsheng Wang[1,2], and Shui Wang[1,2]

[1]School of Earth and Space Sciences, CAS Key Lab of Geospace Environment, University of Science and Technology of China, Hefei, China, [2]CAS Center for Excellence in Comparative Planetology, Hefei, China, [3]Department of Earth, Planetary, and Space Sciences, Institute of Geophysics and Planetary Physics, University of California, Los Angeles, CA, USA, [4]Physics Department, Auburn University, Auburn, AL, USA

Abstract Flux ropes are ubiquitous at Earth's magnetopause and play important roles in energy transport between the solar wind and Earth's magnetosphere. In this study, structure and coalescence of the magnetopause flux ropes formed by multiple X line reconnection in cases with different southward interplanetary magnetic field (IMF) clock angles are investigated by using three-dimensional global hybrid simulations. As the IMF clock angle decreases from 180°, the axial direction of the flux ropes becomes tilted relative to the equatorial plane, the length of the flux ropes gradually increases, and core field within flux ropes is formed by the increase in the guide field. The flux ropes are formed mostly near the subsolar point and then move poleward toward cusps. The flux ropes can eventually enter the cusps, during which their helical structure collapses, their core field weakens gradually, and their axial length decreases. When the IMF clock angle is large (i.e., the IMF is predominantly southward), the flux ropes can coalesce and form new ones with larger diameter. The coalescence between flux ropes can occur both near the subsolar point when they are newly formed and away from the subsolar point (e.g., in the southern hemisphere) when they move toward cusps. However, when the IMF clock angle is small (≤135°), we do not find coalescence between flux ropes.

1. Introduction

Magnetic flux ropes formed at Earth's day-side magnetopause play important roles in the transfer of energy and plasma from the solar wind and the magnetosheath into the magnetosphere through flux transfer events (FTEs). FTEs were first observed by Russell and Elphic (1978) who believed that FTEs are elbow-shaped magnetopause flux ropes formed by magnetic reconnection between the magnetosheath field lines and magnetospheric field lines. On the other hand, Lee and Fu (1985) proposed that FTEs are flux ropes formed by multiple X line reconnection. The model of FTEs as flux ropes formed by multiple X line reconnection was supported by subsequent spacecraft observations studies, which showed that the flux ropes have a helical structure with a strong core field in the axial direction (e.g., Akhavan-Tafti et al., 2018; Paschmann et al., 1982). In the decades that followed, further spacecraft observations provided strong evidence for the formation of flux ropes by multiple X line reconnection (e.g., Fuselier et al., 2018; Hasegawa et al., 2010; Øieroset et al., 2016; Zhong et al., 2013). More recent spacecraft observations have shown that these magnetopause flux ropes can coalesce and form new ones (Alm et al., 2018; Kacem et al., 2018; Wang et al., 2017; Zhou et al., 2017). The coalescence between flux ropes plays an important role because it can accelerate particles effectively (e.g., Oka et al., 2010; Pritchett, 2008; Wang et al., 2016b).

Global-scale simulations have been performed to better understand the structure and coalescence of magnetopause flux ropes. Early global simulations were mostly magnetohydrodynamic (MHD). Using the global MHD simulations, Fedder et al. (2002) showed the typical magnetic field signature of flux ropes and suggested that the flux ropes are formed by nonsteady reconnection along the separator at the magnetopause. Raeder (2006) reported the formation of flux ropes between multiple X lines in a global MHD simulation with large dipole tilt angle, but there was no flux ropes at magnetopause without the dipole tilt angle. However, subsequent global MHD simulations by Dorelli et al. (2009) and Glocer et al. (2016) suggested that flux ropes can also form without a dipole tilt angle. Using multifluid global MHD simulations,

10.1029/2020JA028670

Winglee et al. (2008) showed that the magnetosphere flux ropes formed by multiple X line reconnection can be hundreds to thousands of kilometers in diameter and can expand laterally. In their simulation results, these flux ropes have a strong core magnetic field, and a mixture of magnetospheric and magnetosheath plasma. However, MHD simulations do not include particle kinetics and therefore cannot describe small, kinetic-scale flux ropes and kinetic-scale physics processes.

One way to include particle kinetics into global-scale simulations is embedding a domain of particle-in-cell (PIC) simulation into a global MHD simulation (Tóth et al., 2016) because PIC simulations treat ions and electrons as full particles. Using the MHD with embedded PIC simulations, Chen (2017) studied Earth's magnetopause flux ropes formed by day-side magnetic reconnection and showed that flux ropes can form near the subsolar point and move toward the poles in steady purely southward IMF conditions. Their simulations also showed that two flux ropes can merge at one end and form a new long flux rope near the subsolar point.

Hybrid simulations, in which ions are treated as full particles while electrons are treated as a massless fluid, can also describe ion kinetics in a global context. Using a two-dimensional (2-D) global hybrid simulation, Karimabadi (2006) showed the formation of multiple X lines and copious flux ropes, which contain magnetosheath and magnetosphere plasma under southward IMF. Further 2-D global hybrid simulations by Omidi and Sibeck (2007) and Sibeck and Omidi (2012) showed that small flux ropes would coalesce near the subsolar point and gradually accelerate up to the Alfvén velocity before they move into cusp, and when the flux ropes reach the cusp, reconnection happens between the flux rope magnetic field and the cusp magnetic field lines, thus the flux ropes will be destroyed. Using another type of global hybrid simulation, in which ions kinetics are resolved by solving ion Vlasov equations, Hoilijoki (2017, 2019) studied the effects of magnetosheath fluctuations and IMF tilt on the magnetopause reconnection and flux ropes. However, the flux ropes in magnetopause are of three-dimensional (3-D) nature.

The above global hybrid simulations, however, are 2-D, which assume uniformity and infinite length in the dawn-dusk direction. The first 3-Dglobal hybrid simulation of magnetopause reconnection and flux ropes was performed by Tan et al. (2011). In their simulation, a quadrupole magnetic field signature associated with the Hall effects is found to be present around flux ropes, and flux ropes are formed between finite length X lines and the ion density is enhanced within flux ropes because of the trapped particles, leading to a filamentary global density. Guo et al. (2020) further used global hybrid simulations to study formation and global evolution of magnetopause flux ropes in a magnetospheric multiscale (MMS) event with dipole tilt. These two global hybrid simulation studies only considered a pure southward IMF case. However, the structure and evolution of magnetopause flux ropes are strongly dictated by the IMF orientation or the clock angle, the angle between the geocentric solar-magnetospheric (GSM-z) and projection of IMF on the GSM y-z plane (i.e., the clock angle can be represented as $\tan^{-1}\left(B_y / B_z\right)$) (e.g., Fuselier et al., 2018, 2019; Phan et al., 2006). Therefore, in this study, we examine the structure and evolution of the magnetopause flux ropes and their dependence on the IMF clock angles. The study is organized as follows: The description of the simulation model is in Section 2, the simulation results are presented in Section 3, and Section 4 contains the conclusions and discussion.

2. Simulation Model

Hybrid simulations consider ions as particles and electrons as a massless and charge neutralizing fluid. The global hybrid simulation scheme we use is described by Swift (1996) and applied by Lin and Wang (2005) for 3-D simulations of the dayside magnetosphere. We use the GSM coordinate to describe the simulation results, in which the x axis points from the Earth to the Sun, the positive z axis points to the northern magnetic pole, and the y axis is defined to be perpendicular to the Earth's magnetic dipole from dawn to dusk. However, the spherical coordinate system is used in the simulation. The polar angle θ is measured from the positive GSM z axis, and the azimuthal (longitudinal) angle φ from the negative GSM y axis. Bow shock, magnetosheath, and magnetosphere in the dayside region with a geocentric distance $4\ R_E \le r \le 24\ R_E$ (where R_E is the Earth's radius), polar angle $20° < \theta < 160°$ and azimuth angle $0° < \varphi < 180°$ are all contained in the simulation domain. The Earth is located at the origin $r = 0$. Outflow boundary conditions are utilized at the tailward boundary at $x = 0$, while solar wind inflow boundary conditions are applied at $r = 24\ R_E$. The inner

Table 1
Five Simulation Cases Presented in This Paper, With Different Interplanetary Magnetic Field (IMF) Clock Angle α

Case	A	B_{x0}	B_{y0}	B_{z0}
1	180°	>0	0	−1
2	165°	>0	0.2588	−0.9659
3	150°	>0	0.5	−0.8660
4	135°	>0	0.7071	−0.7071
5	120°	>0	0.8660	−0.5

Note. Case 5 is presented in the supporting information. The magnetic field has been normalized.

boundary at $r = 4\ R_E$ is perfectly conducting. Except for the inner magnetosphere with $r < 7\ R_E$ is dominated by a cold ion fluid, the ions are fully kinetic particles. The Earth's dipole magnetic field is placed in $r \leq 10\ R_E$, and IMF interacted with the former in $r > 10\ R_E$.

The magnetic field B and ion number density N is normalized by the IMF magnitude B_0 and the solar wind density N_0; The time t is normalized by the inverse of the solar wind ion gyrofrequency ($\Omega_{i0}^{-1} = m_i / eB_0$); The flow velocity V is normalized by the solar wind Alfvén speed $V_{A0} = B_0 / \sqrt{\mu_0 m_i N_0}$; the length is expressed in the units of Earth's radius R_E which is ten times ion inertial length $d_{i0} = c / \omega_{pi0} = 0.1\,R_E$ (where $\omega_{pi0} = \left(N_0 e^2 / m_i \varepsilon_0\right)^{1/2}$ is ion plasma frequency) in the solar wind. The global size of the magnetopause (e.g., its standoff distance R_{MP}) is determined by the Mach number and the geomagnetic dipole strength. In the present simulation, the Mach number, ion β_i value, the dipole field strength, and thus R_{MP} all have the realistic values. On the other hand, in order to accommodate to the computation resource, the solar wind ion inertial length d_{i0} in our simulations is several times larger than the realistic value. If we consider a typical interplanetary magnetic field B_0 = 10 nT and a typical solar wind density $N_0 = 6\,\text{cm}^{-3}$ in the solar wind, then the realistic $d_{i0} = 93.1\,\text{km} \approx 0.015\,R_E$, $V_{A0} = 89\,\text{km / s}$, and $\Omega_{i0} = 0.96\,\text{s}^{-1}$. In our simulations, we use $d_{i0} = 0.1 R_E$ (about 6 times larger than the realistic d_{i0}). Therefore, the Alfvén velocity and the global time in our simulations also need to be about 6 times larger (Lin et al., 2014). Our choice of the realistic R_{MP} and larger-than-realistic d_{i0} leads to a scaled d_{i0}/R_{MP}. There is another way of scaling d_{i0}/R_{MP} by keeping d_{i0} realistic and adopting a smaller dipole field and thus a smaller R_{MP}. It has already been shown that the scaling of d_{i0}/R_{MP} does not affect the global structure of the magnetosphere (e.g., Omidi et al., 2004; Tóth et al., 2017).

A total grid $N_r \times N_\varphi \times N_\theta$ = 220 × 114 × 130 is used in the simulation. In order to produce a higher resolution near the magnetopause, nonuniform grids are used in the r direction with a smaller grid size of $\Delta r = 0.025\,R_E$ limited to $8\,R_E \leq r \leq 10\,R_E$. The time step is $\Delta t = 0.05\Omega_{i0}^{-1}$ and there is a total of $\sim 8 \times 10^8$ particles in the simulation. We use a small current-dependent collision frequency, $\upsilon = 0.02\Omega_i J / J_0$, to simulate the special anomalous resistivity and trigger magnetic reconnection at the magnetopause, where J is the current density, Ω_i is local ion gyro-frequency and $J_0 = B_0 / \mu_0 d_{i0}$.

The ion and electron plasma beta in the solar wind is $\beta_i = \beta_e = 0.5$, and the Alfvén Mach number is M_A = 5. The ion number density in the solar wind is set to be $N_0 = 11000\,R_E^{-3}$ and the solar wind plasma will flow into the simulation domain along the -x direction with an isotropic drifting-Maxwellian distribution.

The IMF is assumed to be $\mathbf{B}_0 = \left(B_x, B_y, B_z\right) = \left(0, \sin\alpha, \cos\alpha\right)$, and α (IMF clock angle) is defined as the angle between the GSM-z and projection of IMF in the GSM y-z plane (i.e., the clock angle can be represented as $\tan^{-1}\left(B_y / B_z\right)$), with α = 180° referring to a purely southward IMF. Five cases with different southward IMF clock angle (α = 180°, 165°, 150°, 135°, 120°) are presented in this paper, as shown in Table 1.

3. Simulation Results

3.1. Case 1: Clock Angle of 180°

In this pure southward IMF case, after $\Omega_{i0}t$ = 15, flux ropes begin to form at the magnetopause as the IMF reconnects with the Earth's dipole field. Figure 1 shows the ion plasma density N_i in the meridian plane at $\Omega_{i0}t$ = 26, 36, 46, and 56 obtained from Case 1. The black lines are 2-D magnetic field lines projected onto the noon-midnight meridian plane. Identified using the 2-D field lines projected onto the meridian plane, there is a total of 6 flux ropes (FR_1 through FR_6) formed at $\Omega_{i0}t$ = 26. The enhanced ion density within the flux ropes is clearly shown in Figure 1. Two new flux ropes, FR_7, and FR_8, are formed north of the subsolar point at $\Omega_{i0}t$ = 36, and two more flux ropes (FR_9, FR_{10}) are formed by $\Omega_{i0}t$ = 56. Therefore, we can roughly estimate that in this simulation, a flux rope is formed approximately every 10 Ω_{i0}^{-1} after the first reconnection is triggered. There is little difference in the number or characteristics of flux rope between the northern and southern hemispheres. Note that the northern-southern symmetry exists because we do not have

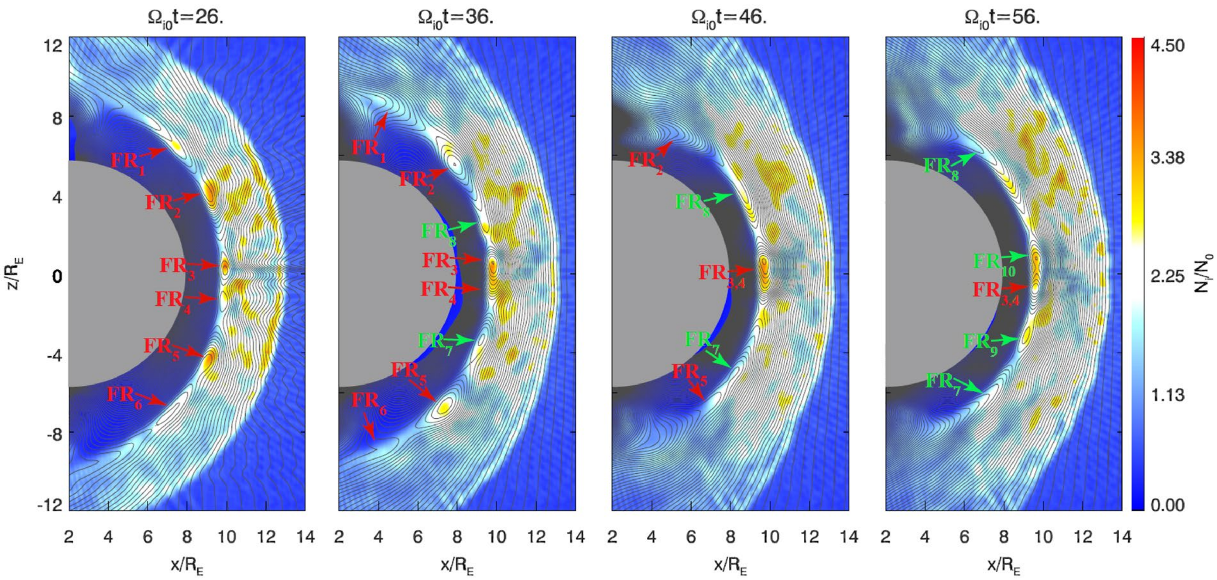

Figure 1. The distribution of the ion density N_i in the noon-midnight meridian plane obtained from Case 1 at $\Omega_{i0}t$ = 26, 36, 46, and 56. The magnetic field lines are superposed in the figure with the black lines. The red letters and arrows represent the flux ropes that have formed at Ω_{i0} = 26 and the green letters and arrows represent the ones formed later.

dipole tilt in our simulations. When there is a substantial dipole tilt, the flux ropes and X lines would shift from the subsolar point to northern or southern hemisphere (Guo et al., 2020). Some flux ropes formed at subsolar point stay there for a while (about $30\Omega_{i0}^{-1}$). Just like FR_3 and FR_4, they coalesce at $\Omega_{i0}t = 26$, and the coalescence is completed at $\Omega_{i0}t = 46$ to form a larger flux rope $FR_{3,4}$, which does not leave the subsolar point until $\Omega_{i0}t = 56$.

Figure 2 shows the structure and evolution of FR_2 (red and blue magnetic field lines) and FR_6 (yellow and green magnetic field lines) from the 3-D perspective. The magnetic field B_y in the noon-midnight meridian plane at $\Omega_{i0}t = 28, 36,$ and 46 is also shown in Figure 2. Some flux ropes formed on both sides of the subsolar

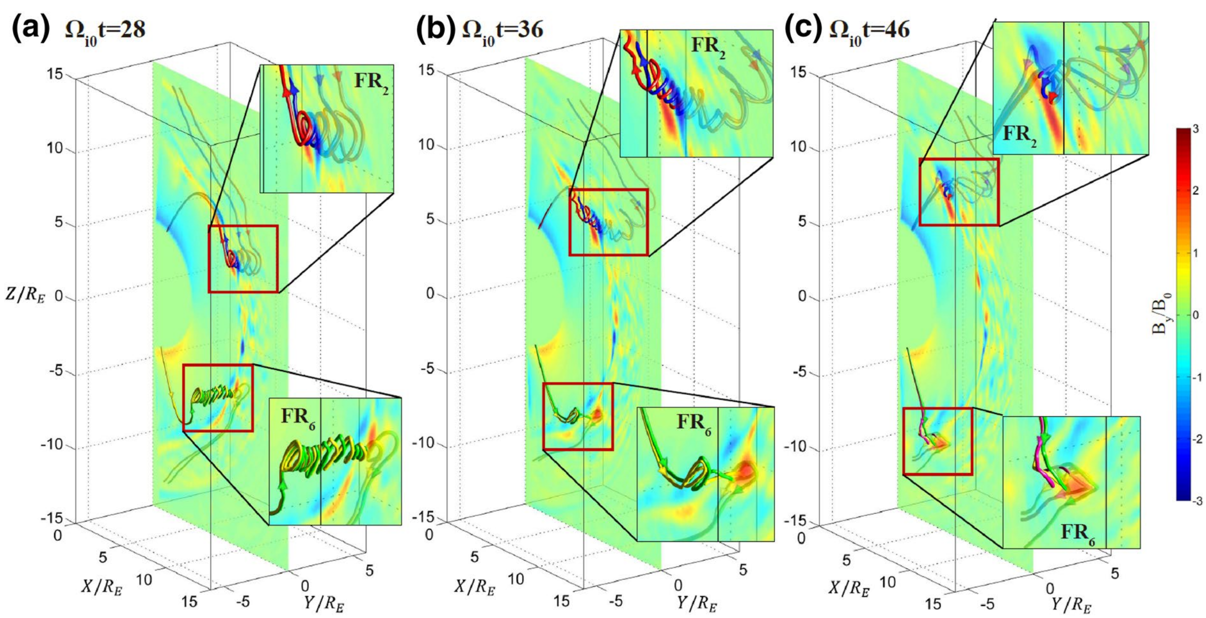

Figure 2. The distribution of magnetic field strength B_y in the noon-midnight meridian plane obtained from Case 1 at $\Omega_{i0}t$ = 28, 36, and 46. The structure of FR_2 (red and blue magnetic field lines) and FR_6 (yellow and green magnetic field lines) from 3-D perspective are shown in the figure.

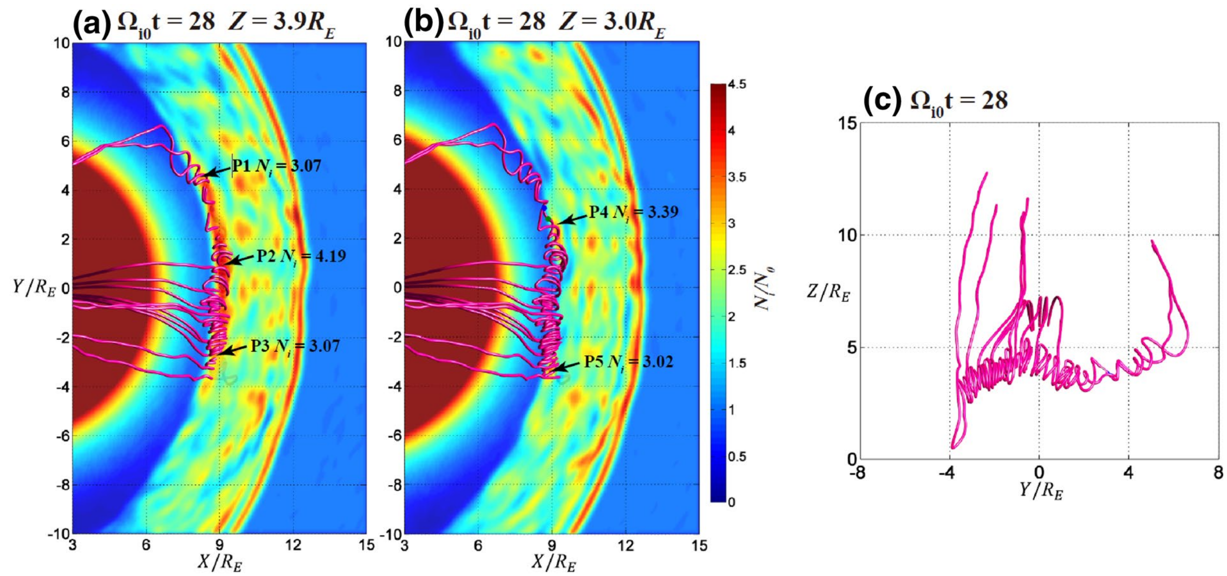

Figure 3. (a) and (b) The distribution of ion density N_i and 3-D magnetic field lines of FR_2 in the *x*-*z* plane obtained from Case 1 at $\Omega_{i0}t = 28$. (c) 3-D magnetic field lines of FR_2 in the *y*-*z* plane at $\Omega_{i0}t = 28$.

point gradually move toward the north and south cusp regions and eventually disappear in the cusp regions. For example, at $\Omega_{i0}t = 28$, the newly formed flux ropes with helical magnetic field lines are near the equatorial plane, and they gradually move poleward to the cusp regions. As the flux ropes move, their structure changes. FR_2 becomes curved in the dawn-dusk direction at $\Omega_{i0}t = 36$. Eventually, the structure of flux ropes is destroyed in the cusp at $\Omega_{i0}t = 46$. There is a positive and negative B_y structure on both sides of the flux ropes, which is consistent with the Hall magnetic field pattern due to the ion kinetic effects. Asymmetric reconnection occurs at the magnetopause, and the resultant Hall pattern is dominated on the magnetosheath side (the quadrupole B_y perturbations near the subsolar point is more obvious), which is consistent with previous simulations (e.g., Birn et al., 2008; Guo et al., 2020; Karimabadi et al., 1999; Pritchett, 2001; Tan et al., 2011).

Using 3-D field lines and the enhancement of the ion density within flux ropes, we can estimate the length of flux ropes in dawn-dusk direction. Figure 3 shows the distribution of ion density N_i and 3-D magnetic field lines of FR_2 in Case 1. Since FR_2 is bending in the axial direction (see Figure 3c), we show the distribution of ion density in the $z = 3.9\ R_E$ and $z = 3.0\ R_E$ planes. Combining the ion density and the helical structure of FR_2, we consider points P1 and P5 to be the two endpoints of FR_2. The ion density in the FR_2 is higher than the ion density at P1 and P5. In other words, beyond the two points (P1 and P5), the helical structure of FR_2 is no longer exists, and the ion density is less than 3 N_0. The ion density outside of FR_2 is approximately 1–3 N_0, and the ion density inside of FR_2 is approximately 3–5N_0 (these values may slightly differ from one flux rope to another or the same flux rope at different time). Generally speaking, we need the ion density in the flux rope to be 1–2 N_0 higher than background density to determine the length of a flux rope. Thus, the length of FR_2 is about 7.8 R_E at $\Omega_{i0}t = 28$, about 6.8 R_E at $\Omega_{i0}t = 36$, and about 4.8 R_E at $\Omega_{i0}t = 46$; the length of FR_6 is about 6.7 R_E at $\Omega_{i0}t = 28$, about 5.6 R_E at $\Omega_{i0}t = 36$, and FR_6 has completely collapsed at $\Omega_{i0}t = 46$. (Note that FR_2 and FR_6 in Figure 2 show only partial structures in the direction of dawn-dusk.)

FR_3 and FR_4 are coalescing at $\Omega_{i0}t = 26$. The coalescence is completed at $\Omega_{i0}t = 46$, which forms a new flux rope $FR_{3,4}$ (see Figure 1). Figure 4 shows representative magnetic field lines and contours of ions velocity V_z (the *z*-component ion flow velocity) near the noon-midnight meridian plane to demonstrate the process of coalescence between FR_3 and FR_4. The ion density N_i, ion velocity V_z and the flux ropes in the *y*-*z* plane are also shown in a zoomed-in view. The green and red magnetic field lines represent FR_3 and FR_4, respectively. The ion flow is predominantly northward in the northern hemisphere and southward in the southern hemisphere. Upon a closer examination, however, there is regional ion flow perturbation (relative ion flows formed by multiple X line reconnection) near the subsolar point. The ion velocity below FR_4 is positive, and the ion velocity above FR_3 is negative at $\Omega_{i0}t = 18$ and 26, thus, the two flux ropes move toward each other

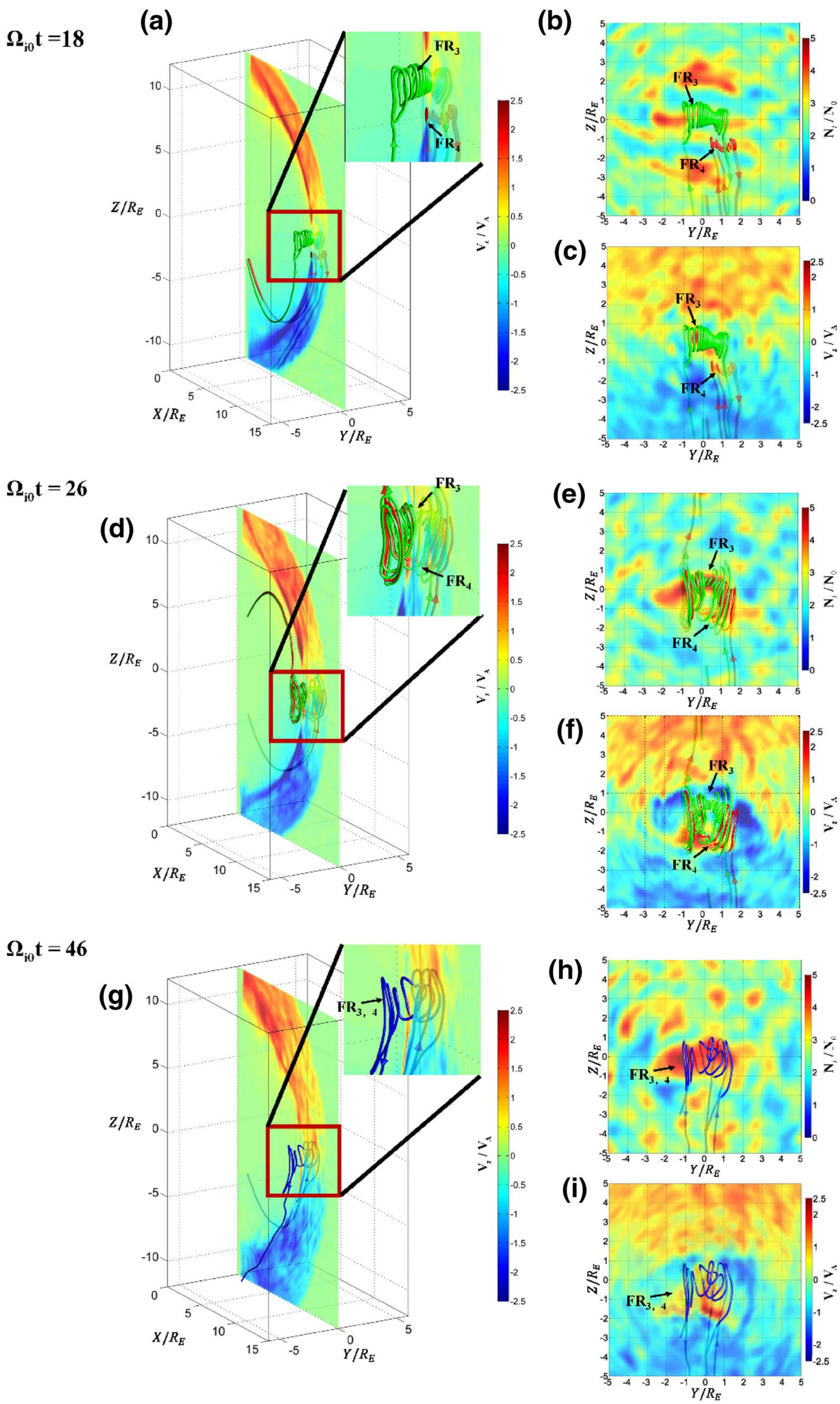
$\Omega_{i0}t$ =18
(a)
(b)
(c)
$\Omega_{i0}t$ = 26
(d)
(e)
(f)
$\Omega_{i0}t$ = 46
(g)
(h)
(i)
FR_3
FR_4
$FR_{3,4}$
Z/R_E
X/R_E
Y/R_E
V_z/V_A
N_i/N_0

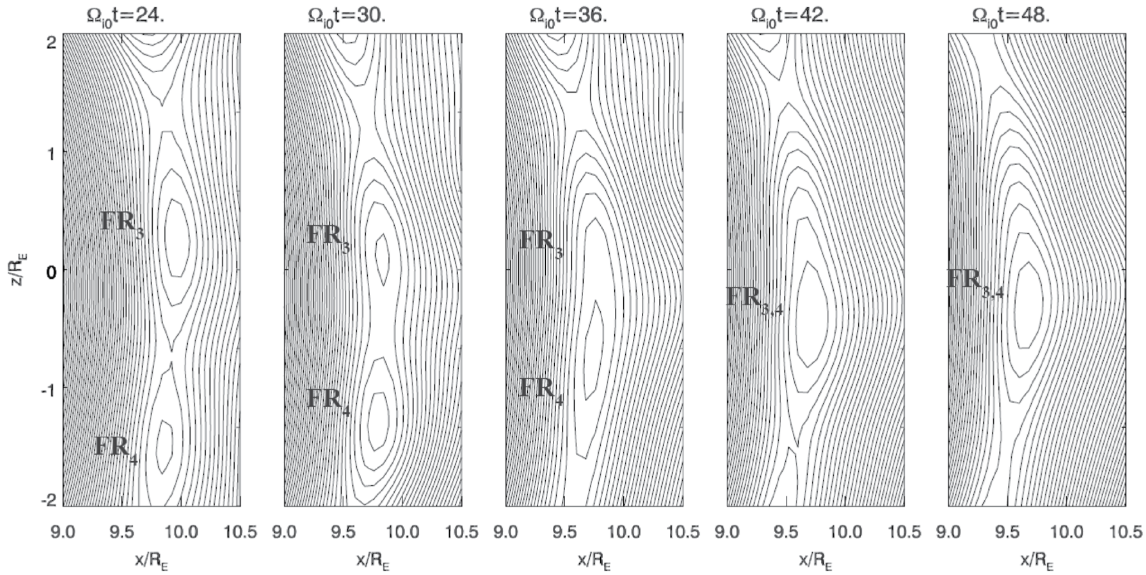

Figure 5. 2-D magnetic field lines at the subsolar point in the $y = 0.36\ R_E$ plane obtained from Case 1 at $\Omega_{i0}t = 24$, 30, 36, 42, and 48.

and a re-reconnection between the two flux ropes occurs, resulting in a coalescence between them. The same result is also shown in the *y*-*z* plane (Figures 4c, 4f, and 4i).

The coalescence process is better shown in Figure 5: FR_3 (northern) and FR_4 (southern) gradually approach each other, and eventually coalesce to form a large flux rope. During the process, the topologies of the magnetic field lines change, showing that the coalescence is through reconnection (or called re-reconnection). Note that the coalescence process between FR_3 and FR_4 is inhomogeneous in the *y* (dawn-dusk) direction, which coalescence occurs first at the two ends of the two flux ropes (Figure 4d) and then proceeds to the middle part (Figure 4g). We also find that there are ion density filaments inside the flux ropes (Figures 4b, 4e, and 4h), and as a result of flux ropes coalescence, the two ion density filaments merge into a new one inside the flux rope $FR_{3,4}$ (blue magnetic field line at $\Omega_{i0}t = 46$). The diameter of FR_3 and FR_4 near noon-midnight meridian plane is about 1.5 R_E and 1 R_E (Figure 4b) respectively, and the diameter of $FR_{3,4}$ which formed by the coalescence between FR_3 and FR_4 is about 2 R_E (Figure 4h). The flux rope coalescence region is about 2.5 R_E in the dawn-dusk direction.

3.2. Case 2: Clock Angle of 165°

The magnetic field lines and ion plasma density N_i in the meridian plane at $\Omega_{i0}t = 26$, 36, 46, and 56 in Case 2 are shown in Figure 6. There is no significant difference in the number of flux ropes formed in the northern and southern hemispheres. The generation and movement of flux ropes are in the same way as Case 1 (under pure southward IMF). However, the structure of the flux ropes and the coalescence process of the flux ropes are somewhat different. FR_7 is formed after FR_3, and then moves toward FR_3. At $\Omega_{i0}t = 61$, a larger flux rope, $FR_{3,7}$ is formed by the coalescence between FR_3 and FR_7. In this case, the coalescence starts and ends at about $\Omega_{i0}t = 46$ and $\Omega_{i0}t = 61$, respectively, which are about $20\Omega_{i0}^{-1}$ later than that in the pure southward IMF. Similar to Case 1, FR_3 stays at the subsolar point for $30\Omega_{i0}^{-1}$ after it is formed at $\Omega_{i0}t = 31$.

Figure 7 shows detailed structures of FR_4 (red and blue magnetic field lines) and FR_5 (yellow, green and violet magnetic field lines) from the 3-D perspective and depicts the contours of magnetic field B_y at $\Omega_{i0}t = 41$, 51, and 66. The helical field line structure of FR_5 has disintegrated at $\Omega_{i0}t = 41$ and will gradually disappear

Figure 4. (a), (d), and (g) Contours of ion velocity V_z near the noon-midnight meridian plane at $\Omega_{i0}t = 18$, 26, and 46, respectively, obtained from Case 1. The right of each figure is a zoom-in view. (b) Contours of ion density N_i in the *y*-*z* plane at $x = 9.9R_E$, $\Omega_{i0}t = 18$. (c) Contours of ion velocity V_z at $x = 9.88R_E$, $\Omega_{i0}t = 18$. (e) Contours of N_i at $x = 10R_E$, $\Omega_{i0}t = 26$. (f) Contours of V_z at $x = 9.8R_E$, $\Omega_{i0}t = 26$. (h) Contours of N_i at $x = 9.8R_E$, $\Omega_{i0}t = 46$. (i) Contours of V_z at $x = 9.5R_E$, $\Omega_{i0}t = 46$. The green and red magnetic field lines represent FR_3 and FR_4, respectively. The blue magnetic field line represents the coalesced flux rope $FR_{3,4}$.

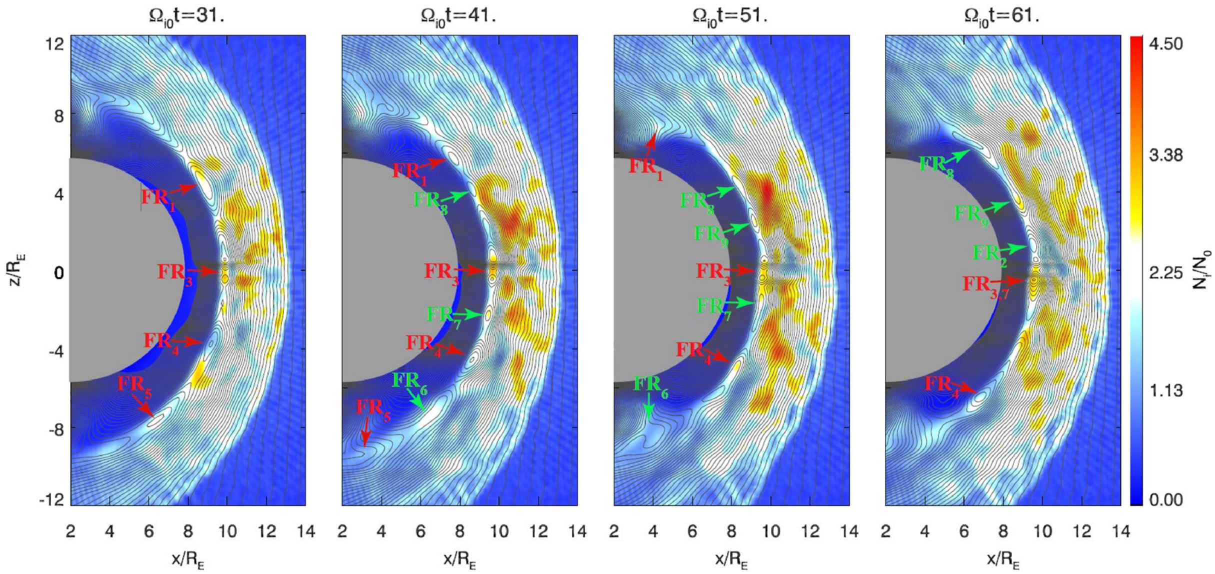

Figure 6. The distribution of the ion density N_i in the noon-midnight meridian plane obtained from Case 2 at $\Omega_{i0}t = 31$, 41, 51, and 61. Same format as in Figure 1.

in cusp. At $\Omega_{i0}t = 51$, there is no trace of FR_5. The magnetic field B_y is no longer quadrupolar at the flux ropes but has an enhancement in the central region of the flux ropes. For example, FR_8, FR_9, and $FR_{3,7}$ (formed by the coalescence between FR_3 and FR_7) all have a strong core magnetic field B_y. The core field of flux ropes is weak at the beginning, and then becomes stronger gradually (see FR_8 and FR_9 in Figures 7b and 7c). The length of FR_4 is about $4.4R_E$ at $\Omega_{i0}t = 41$, about $8R_E$ at $\Omega_{i0}t = 51$, and about $3R_E$ at $\Omega_{i0}t = 66$; the length of FR_3 is about $6R_E$ at $\Omega_{i0}t = 41$, about $6R_E$ at $\Omega_{i0}t = 51$, and about $7R_E$ at $\Omega_{i0}t = 66$ ($FR_{3,7}$). The length of FR_7 is about $2R_E$ when it is just formed at $\Omega_{i0}t = 38$.

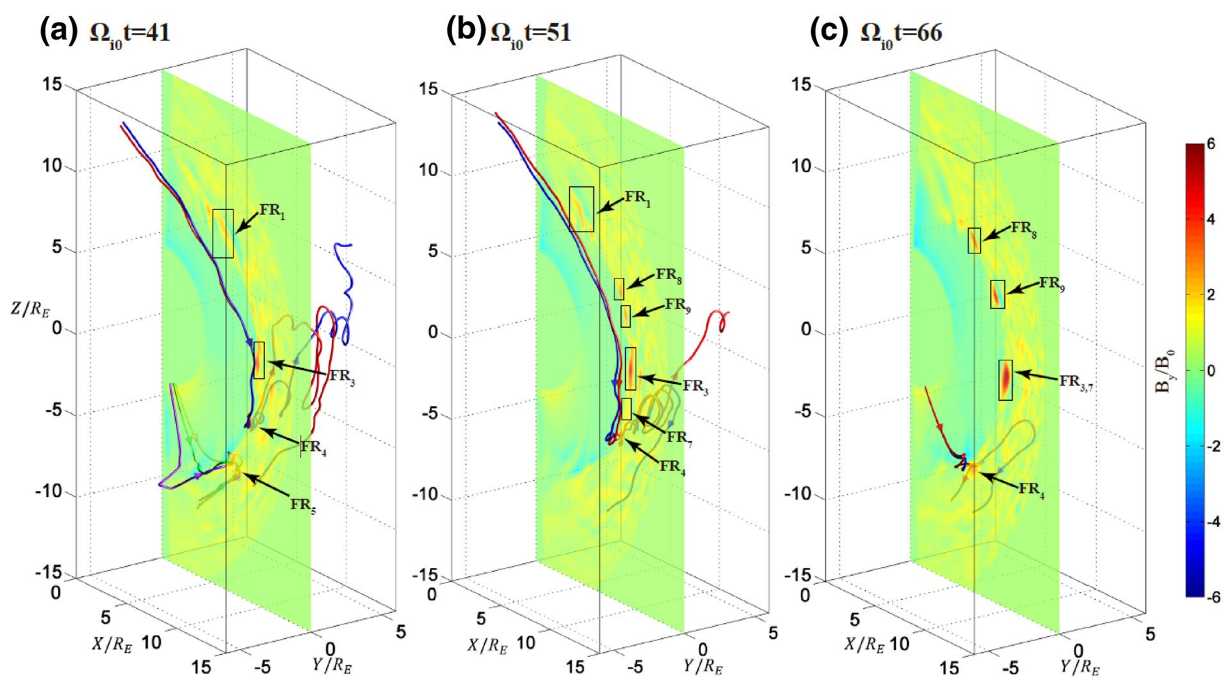

Figure 7. The distribution of magnetic field strength B_y in the noon-midnight meridian plane obtained from Case 2 at $\Omega_{i0}t = 41$, 51, and 66. The structure of FR_4 (red and blue magnetic field lines) and FR_5 (yellow, green and violet magnetic field lines) from 3-D perspective are shown in the figure. Flux ropes that are not represented by magnetic field lines are marked by black rectangles to indicate their positions.

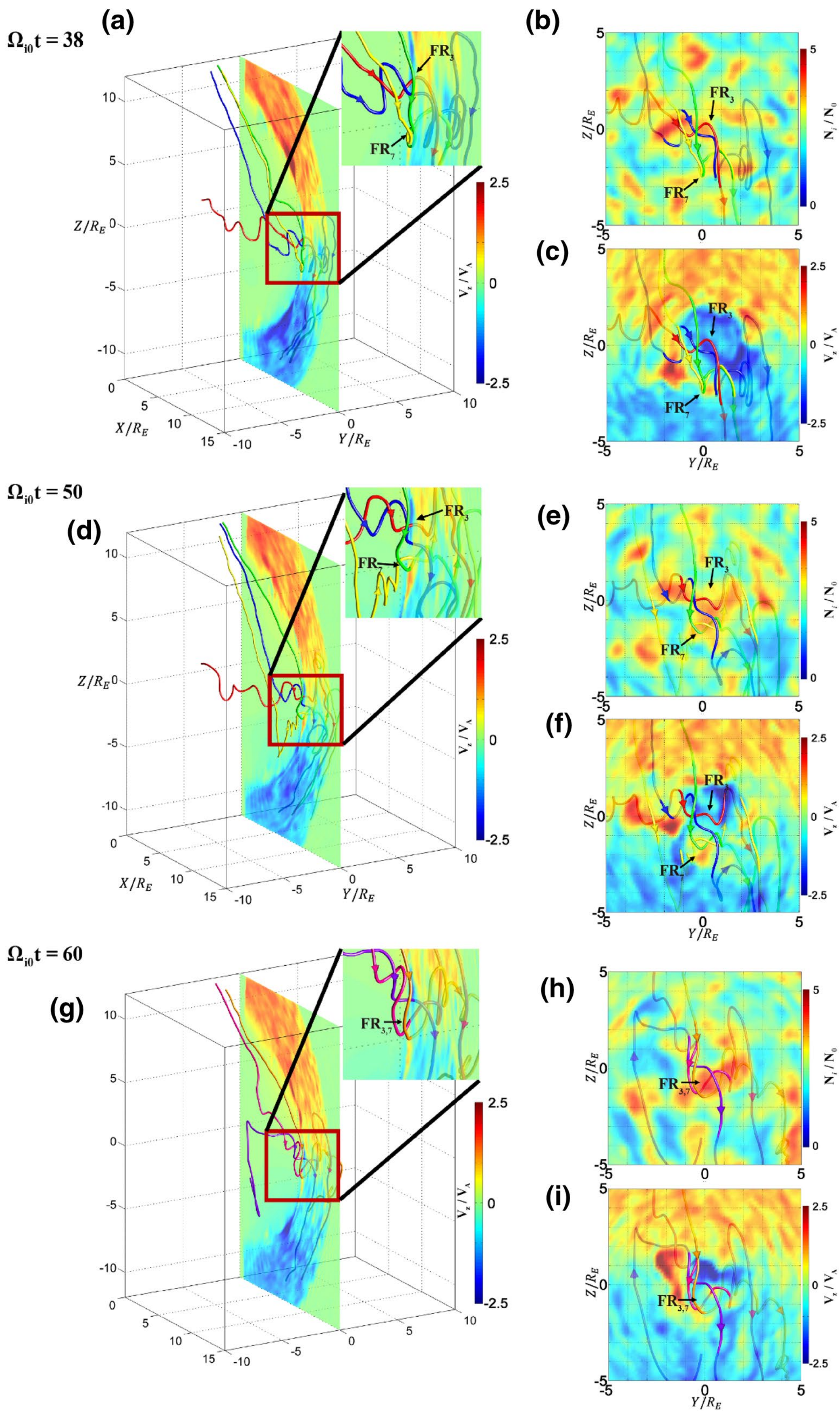
(a)
$\Omega_{i0}t = 38$
(b)
(c)
$\Omega_{i0}t = 50$
(d)
(e)
(f)
$\Omega_{i0}t = 60$
(g)
(h)
(i)
FR3
FR7
FR3,7
Z/R_E
X/R_E
Y/R_E
V_z/V_A
N_i/N_0
2.5
0
-2.5
5
0
-5
10
-10
15

10.1029/2020JA028670

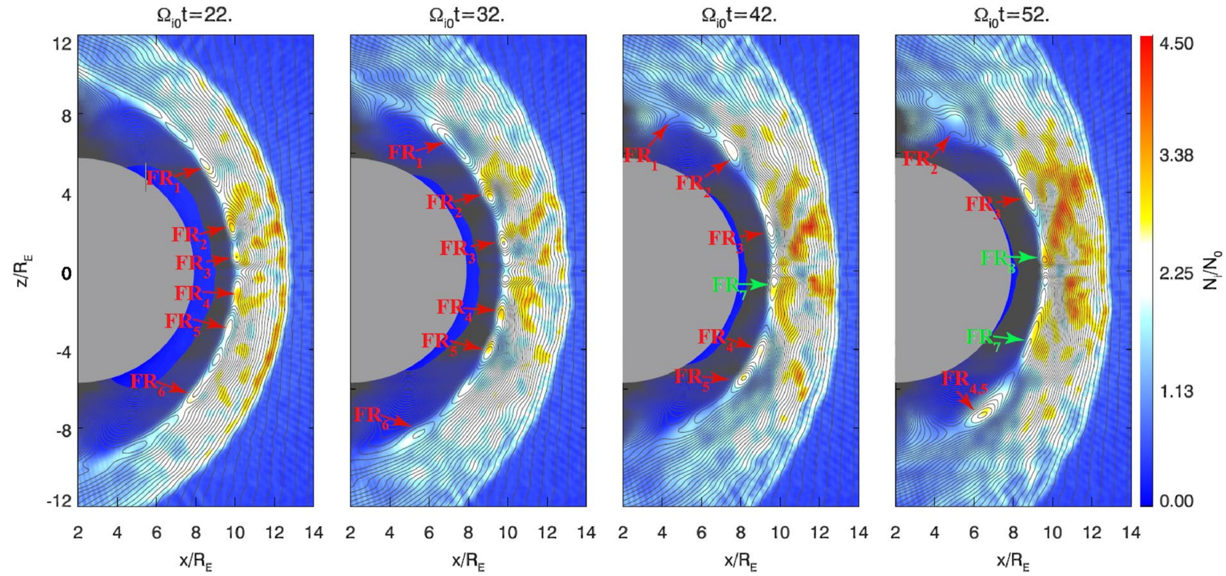

Figure 9. The distribution of the ion density N_i in the noon-midnight meridian plane obtained from Case 3 at $\Omega_{i0}t$ = 22, 32, 42, and 52. Same format as in Figure 1.

The coalescence between FR_3 (red and blue magnetic field lines) and FR_7 (yellow and green magnetic field lines) is shown in Figure 8. FR_7 is formed between FR_3 and FR_4, later than FR_3 and slightly smaller than FR_3 (Figure 8a). Upon a closer examination of the ion velocity V_z in the noon-midnight meridian plane (Figure 8), there are also ion flows regional perturbation caused by reconnection outflows from multiple X lines near the subsolar point, which is similar to Case 1. After the formation of FR_7, it is pushed northward by the positive high-speed flow. At the same time, FR_3 moves southward because of the strong negative flow. Therefore, FR_3 and FR_7 move toward each other and then begin to coalesce at $\Omega_{i0}t = 50$. Figure 8e shows that the merging of the two ion density filaments occurs near the subsolar point. The diameter of FR_3 and FR_7 near noon-midnight meridian plane is about $1R_E$ and $0.5R_E$ (Figure 8b), respectively, and the diameter of $FR_{3,7}$ is about $1.5R_E$ (Figure 8h). The flux rope coalescence region is about $2.5R_E$ in dawn-dusk direction.

3.3. Case 3: Clock Angle of 150°

The generation and evolution of the flux ropes in Case 3 (IMF clock angle of 150°) is shown in Figure 9. Six flux ropes, FR_1–FR_6 have been formed by $\Omega_{i0}t = 22$. The six flux ropes move toward the north or south cusp, driven by the plasma flow, which is similar to Cases 1 and 2. FR_4 and FR_5 gradually coalesce, which forms $FR_{4,5}$. This flux ropes coalescence occurs at ($\Omega_{i0}t = 32$), later than that in Cases 1. Unlike Cases 1 and 2, the flux ropes formed at the subsolar point stay there less than $10\Omega_{i0}^{-1}$. Just like FR_3, FR_4, and FR_7, they leave subsolar point quickly and move toward the cusp regions.

The structure of FR_1 (yellow, green and violet magnetic field lines) and FR_2 (red and blue magnetic field lines) from the 3-D perspective and magnetic field B_y in the noon-midnight meridian plane at $\Omega_{i0}t = 28, 36, \textit{and } 46$ are shown in Figure 10. FR_2 is formed at $\Omega_{i0}t = 22$ and the core field B_y is weak. As FR_2 moves northward, its core field B_y becomes progressively stronger and the region of enhancement becomes larger (see Figures 10b and 10c). Note that the axial direction of the flux ropes in Cases 1 and 2 is almost parallel to the equatorial plane, but FR_2 in Case 3 tilts counterclockwise for about 14° from equatorial plane at $\Omega_{i0}t = 22$. The length of FR_1 is about 6.1 R_E at $\Omega_{i0}t = 22$, and then it has completely collapsed at $\Omega_{i0}t = 40$; the length

Figure 8. (a), (d), and (g) Contours of ions velocity V_z in the noon-midnight meridian plane at $\Omega_{i0}t = 38$, 50, and 60, respectively, obtained from Case 2. The right of each figure is a zoom-in view. (b) Contours of ion density N_i in y-z plane at $x = 9.55R_E$, $\Omega_{i0}t = 38$. (c) Contours of ion velocity V_z at $x = 9.5R_E$, $\Omega_{i0}t = 38$. (e) Contours of N_i at $x = 9.45R_E$, $\Omega_{i0}t = 50$. (f) Contours of V_z at $x = 9.35R_E$, $\Omega_{i0}t = 50$. (h), (i) Contours of N_i and V_z at $x = 9.5R_E$, $\Omega_{i0}t = 60$. Blue and red magnetic field lines represent FR_3. Yellow and green magnetic field lines represent FR_7. The coalesced flux rope $FR_{3,7}$ is represented by orange, pink and violet magnetic field lines.

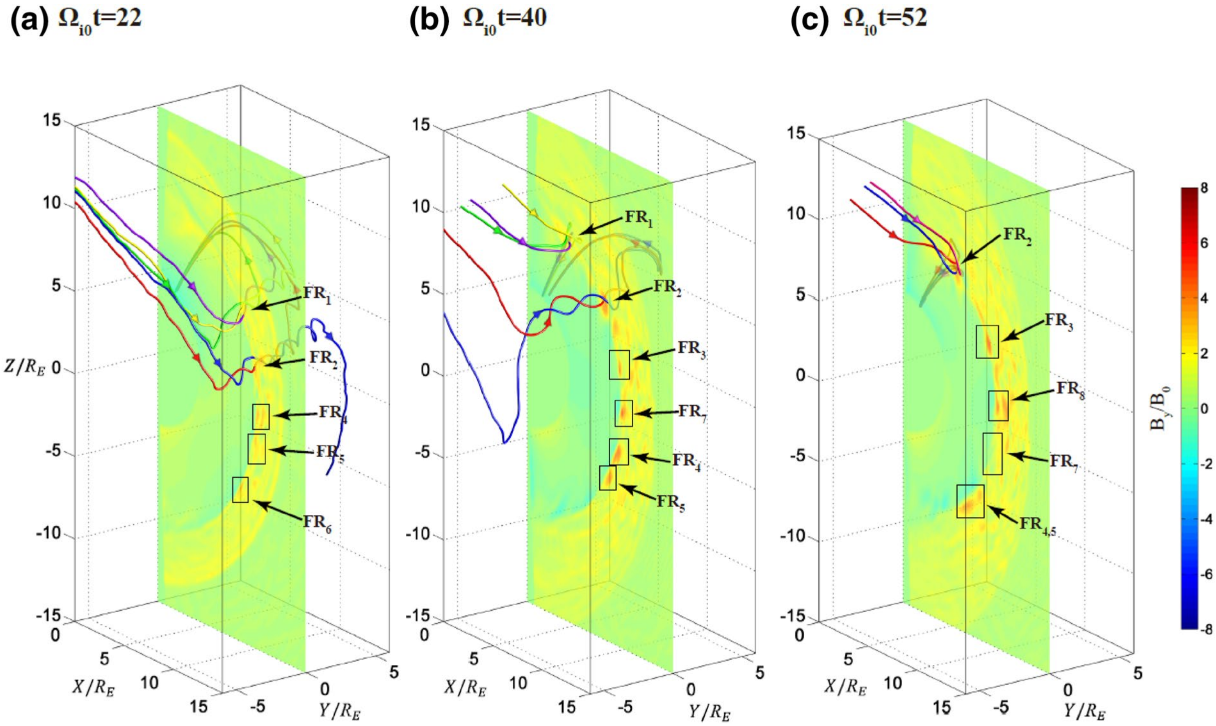

Figure 10. The distribution of magnetic field strength B_y in the noon-midnight meridian plane obtained from Case 3 at $\Omega_{i0}t$ = 22, 40, and 50. The structure of FR_1 (yellow, green and violet magnetic field lines) and FR_2 (red and blue magnetic field lines) from 3-D perspective are shown in the figure. FR_2 at $\Omega_{i0}t = 50$ is represented by red, blue and pink magnetic field lines to show its detailed structure. The locations of other flux ropes are marked with black rectangles and arrows.

of FR_2 is about 7 R_E at $\Omega_{i0}t = 22$, about 4.7 R_E at $\Omega_{i0}t = 40$, and it has completely collapsed at $\Omega_{i0}t = 52$. More interestingly, $FR_{4,5}$ formed by coalescence can extend up to 10 R_E in the axial direction.

The coalescence process between FR_4 and FR_5 is shown in Figure 11, in which the blue and red magnetic field lines represent FR_4, the yellow and green magnetic field lines represent FR_5, and $FR_{4,5}$ is represented by orange, pink and violet magnetic field lines at $\Omega_{i0}t = 52$. By checking of the ion velocity V_z in the noon-midnight meridian plane in Figure 11, the regional ion flow perturbation near the subsolar point caused by reconnection outflows from multiple X lines is not obvious. The coalescences in Cases 1 and 2 occurs near the subsolar point, but the coalescence in Case 3 occurs during flux ropes move toward the south cusp region. FR_4 and FR_5 are formed at about $\Omega_{i0}t = 22$, and the coalescence between them begins at about $\Omega_{i0}t = 32$. At about $\Omega_{i0}t = 52$, the newly formed $FR_{4,5}$ by the coalescence between FR_4 and FR_5 is at about $z = -7R_E$ in the noon-midnight meridian plane. It is obvious that the ion flow velocity at FR_4 is much faster than that at FR_5. The difference in the ion flow velocity between the two flux ropes results in FR_4 gradually catching up with FR_5 (Figures 11b and 11c). The two flux ropes begin to coalesce first at the dawn end ($\Omega_{i0}t = 32$), then at the dusk end ($\Omega_{i0}t = 42$), and finally near the noon-midnight meridian plane ($\Omega_{i0}t = 52$). The diameter of FR_4 and FR_5 is about $1R_E$ near noon-midnight meridian plane (Figure 11a), and that of $FR_{4,5}$ formed by the coalescence between FR_4 and FR_5 is about $3R_E$ (Figure 11d). The length of FR_4 and FR_5 is about 11 R_E and 7 R_E, respectively, at $\Omega_{i0}t = 42$, and the length of the $FR_{4,5}$ formed by the coalescence between FR_4 and FR_5 can be up to $13R_E$. As $FR_{4,5}$ moves south toward cusp region, the length of $FR_{4,5}$ become shorter (about $10R_E$) at $\Omega_{i0}t = 52$. In this case, the flux rope coalescence region is about $5R_E$ in dawn-dusk direction, longer than in Cases 1 and 2. Similar to other flux ropes, $FR_{4,5}$ eventually enter the cusp region and gradually collapse.

There are three more coalescences in Case 3:

(1) $y = -4–0R_E$, $\Omega_{i0}t = 24–36$, Southern Hemisphere;
(2) $y = 4–8R_E$, $\Omega_{i0}t = 20–32$, Southern Hemisphere, near the Equator;
(3) $y = 3–6R_E$, $\Omega_{i0}t = 30–44$, Northern Hemisphere.

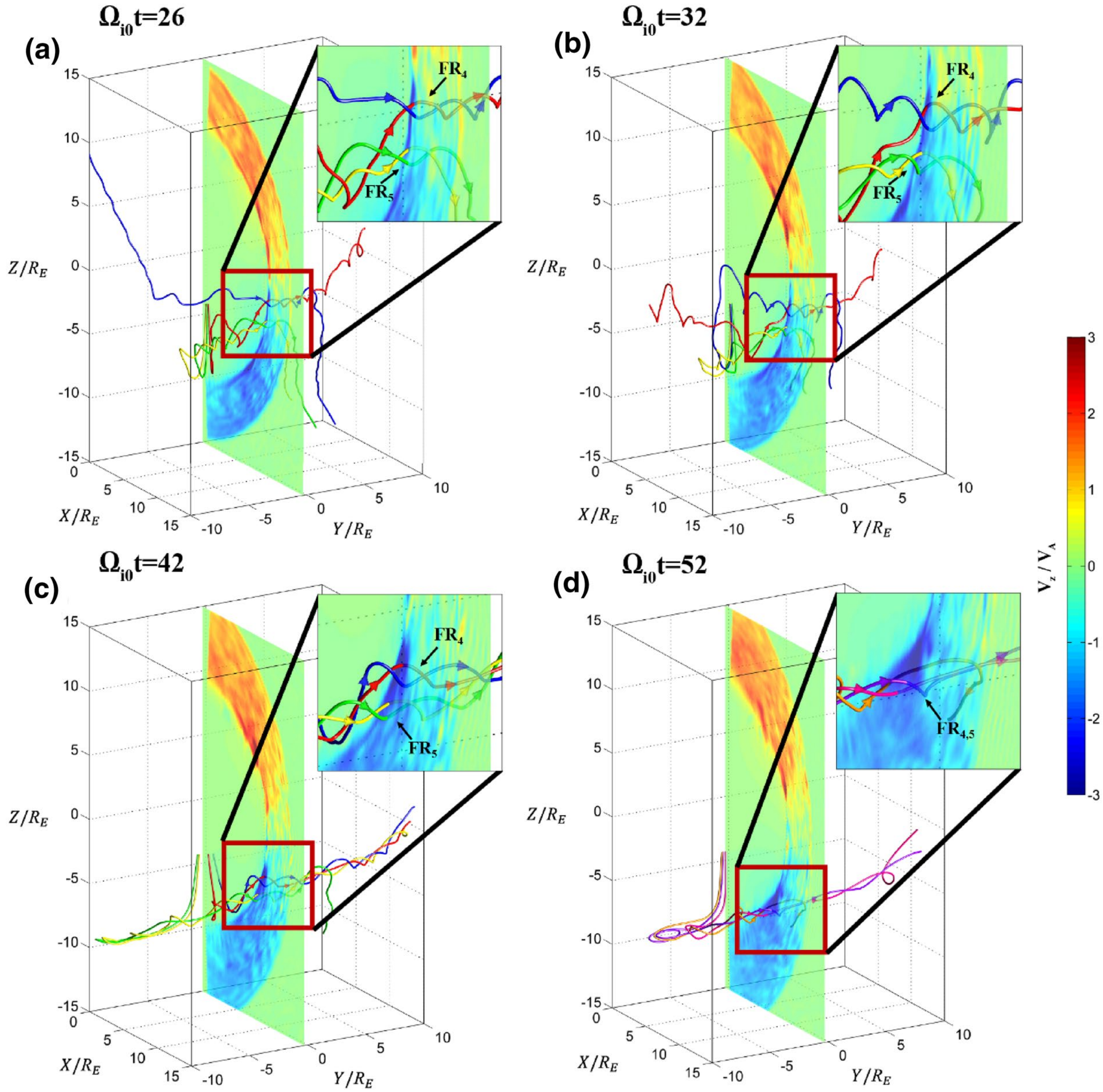

Figure 11. (a)-(d) Contours of ion velocity V_z in the noon-midnight meridian plane at $\Omega_{i0}t$ = 26, 32, 42, and 52, respectively, obtained from Case 3. The right of each figure is a zoom-in view. Blue and red magnetic field lines represent FR_4. Yellow and green magnetic field lines represent FR_5. The coalesced flux rope $FR_{4,5}$ is represented by orange, pink and violet magnetic field lines.

3.4. Case 4: Clock Angle of 135°

Figure 12 shows the generation and evolution of the flux ropes in Case 4 (IMF clock angle of 135°). It can be clearly seen that the ion plasma density in flux rope is smaller than that in the previous three cases. Although there is no significant change in the number of flux ropes compared to the previous cases, no flux ropes coalescence is found in Case 4. Similar to Case 3, flux ropes formed at the subsolar point, such as FR_3 and FR_4, do not stay there for a long time.

The structure of FR_4 (red, blue, and violet magnetic field lines) and FR_5 (yellow, green, and sky-blue magnetic field lines) from the 3-D perspective are shown in Figure 13. In the presence of a strong guide field, the axial length of the flux rope is longer in the dawn-dusk direction. FR_4' axis is tilted relative to the equatorial plane (counterclockwise angle about 20° at $\Omega_{i0}t$ = 25). The sloped flux rope enters cusp region first at its one end

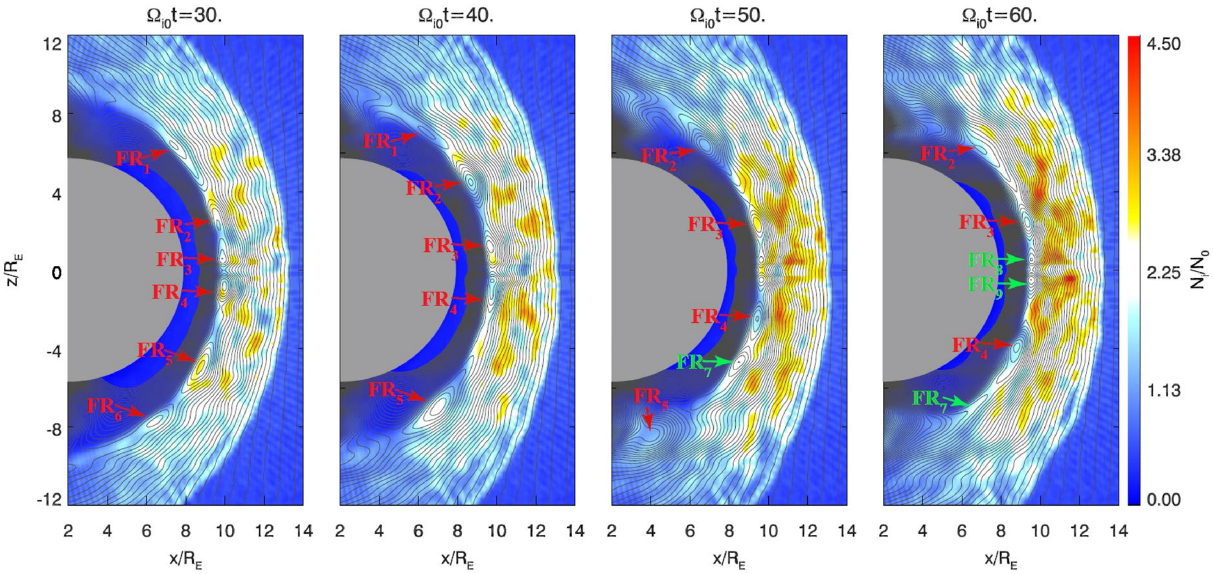

Figure 12. The distribution of the ion density N_i in the noon-midnight meridian plane obtained from Case 4 at $\Omega_{i0}t$ = 30, 40, 50, and 60. Same format as in Figure 1.

and then the rest of it (see FR_5 and FR_7 in Figure 13). The core field in flux ropes is more enhanced in Case 4 than in Cases 2 and 3 (see FR_4 in Figure 13b). To illustrate how much the core field increase approximately, we examine the core field of several representative flux ropes in Cases 2–4, and the results are as follows:

(1) In Case 2, at $\Omega_{i0}t = 41$, FR_3' core field maxima is $4.1B_0$, FR_1' core field maxima is $2.3B_0$, and FR_4' core field maxima is $2.4B_0$
(2) In Case 3, at $\Omega_{i0}t = 40$, FR_7' core field maxima is $5.5B_0$, FR_4' core field maxima is $4.3B_0$, and FR_5' core field maxima is $3.8B_0$

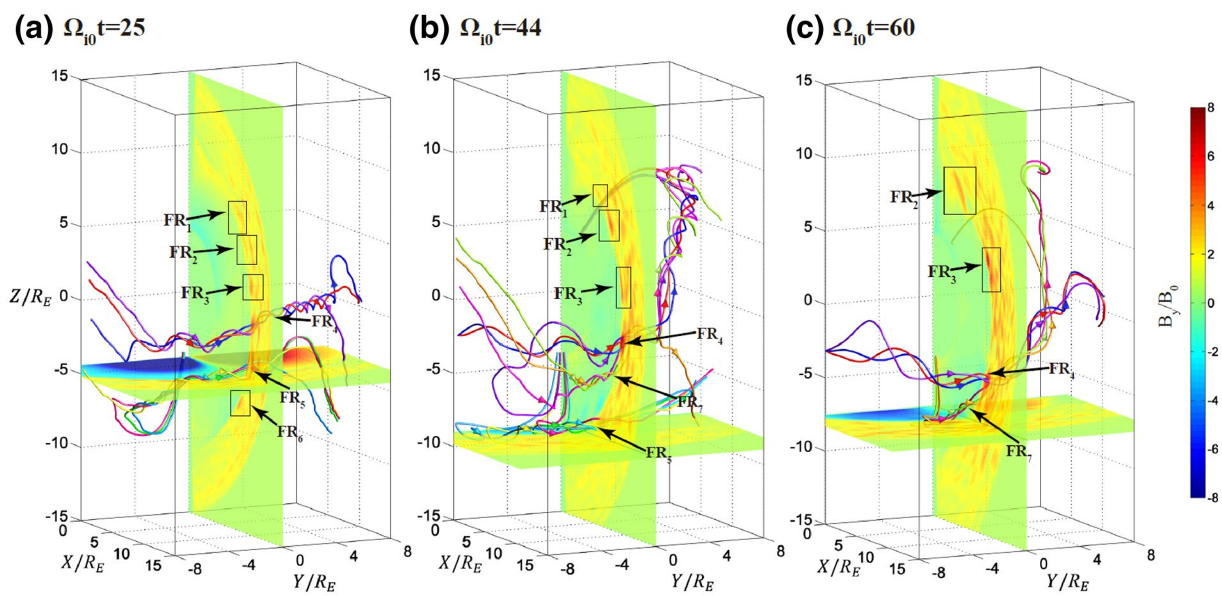

Figure 13. The distribution of magnetic field strength B_y in the noon-midnight meridian plane obtained from Case 4 at $\Omega_{i0}t$ = 25, 44, and 60. The structure of FR_4 (red, blue and violet magnetic field lines) and FR_5 (yellow, green, pink, cyan, and sky blue magnetic field lines) from 3-D perspective are shown in the figure. FR_7 at $\Omega_{i0}t$ = 44, 60 is represented by pink, orange and lime-green magnetic field lines. The location of other flux ropes is also marked with black rectangles and arrows.

(3) In Case 4, at $\Omega_{i0}t = 44$, FR_4' core field maxima is $8.0B_0$, FR_2' core field maxima is $5.2B_0$, and FR_3' core field maxima is $5.5B_0$

It is clear that there is a significant enhancement of the core field with the increase of IMF B_y. FR_7 is formed on the dawn side with one end attached to FR_4 on the dusk side at $\Omega_{i0}t = 44$ (see Figure 13b). As it is just formed, FR_7's core field is not well established, and its core field has increased at $\Omega_{i0}t = 60$. Overall, the flux ropes are longer than those in the previous three cases. The length of FR_4 is about 10 R_E at $\Omega_{i0}t = 25$, about 9 R_E at $\Omega_{i0}t = 40$, and about 8.5 R_E at $\Omega_{i0}t = 60$; the length of FR_6 is about 8 R_E at $\Omega_{i0}t = 25$, about 6.5 R_E at $\Omega_{i0}t = 40$, and it has completely collapsed at $\Omega_{i0}t = 60$.

We have also studied the case with IMF clock angle of 120° (the results are in , Figure S1 and S2) and found no coalescence of flux ropes (like in Case 4). The flux ropes' axis in this case has a large angle relative to the direction of dawn and dusk (counterclockwise angle about 33°, see Figure S2). The axial length of the flux ropes can be up to 12 R_E in the case with IMF clock angle of 120°. By comparing Cases 2–5, we find the flux rope occurrence rate or the number of X lines is basically independent of the clock angle within the time range of our simulations (about 100 Ω_{i0}^{-1}).

4. Conclusions and Discussion

Using 3-D global hybrid simulations, we investigate the structure and coalescence of flux ropes formed by magnetopause reconnection in cases with different southward IMF clock angles. The main results are summarized below:

1. In these simulations, flux ropes formed by multiple X line reconnection has an internal helical magnetic field structure. The presence of guide field causes the flux ropes' axis to tilt relative to the equatorial plane. The B_y quadrupole magnetic field is found in the pure southward IMF (Case 1), and there is a strong core field inside the flux ropes in Cases 2–5 with nonzero IMF B_y values. The core field of flux ropes is weak at the beginning, and then becomes stronger gradually. As the IMF clock angle decreases (guide field increases), the length of the flux ropes gradually increases. The length of flux ropes under pure southward IMF is generally 8 R_E, while those in the IMF clock angle of 120° can be 12 R_E
2. In Cases 1 and 2, the flux ropes formed near the subsolar point stay there for a long time (about 30 Ω_{i0}^{-1}) before they move poleward. However, in Cases 3–5, the flux ropes formed at the subsolar point hardly stay at there, and soon move toward the southern or northern cusp regions. When the flux ropes enter the cusps, their helical structure collapses, their core field weakens gradually, and their length (axial direction) becomes shorter. When the IMF has a nonzero B_y component, sloped flux ropes are formed (i.e., the flux ropes tilt counterclockwise from the equatorial plane). The sloped flux rope enters cusp region first at its one end and then the rest of it
3. The coalescence of the flux ropes is accompanied by the merging of their core fields and ion density filaments. Flux ropes formed by coalescence end up with a larger diameter. In the case of larger IMF clock angles (Cases 1 and 2, $\alpha = 180°, 165°$), flux ropes coalescence occurs only near the subsolar point, but in the case of 150° IMF clock angle, flux rope coalescence occurs when flux ropes move toward the south pole. Flux rope coalescence in Case 3 can form a flux rope of length 13 R_E, and this flux rope is longer than any other flux ropes in this case. The length of the flux ropes coalescence region in Case 3 (longer than 5 R_E in dawn-dusk direction) is longer than that in Cases 1 and 2 (about 2.5 R_E in dawn-dusk direction). When the IMF clock angle is smaller (Cases 4 and 5), flux rope coalescence does not occur

The dependence of magnetopause flux rope characteristics on the IMF clock angle can be understood as the effect of the guide field, i.e., IMF B_y component. The IMF clock angle 180° corresponds to a pure southward IMF with zero guide field, and the guide field B_y increase as the clock angle decreases. Our simulations show that in the pure southward IMF case with zero guide field, the flux ropes have weak core field, while as the clock angle decreases, the core field increases in the flux ropes because the guide field B_y increases, which is consistent with previous local-scale simulations (Karimabadi et al., 1999; Lu et al., 2020). The guide field also controls the axial direction of the X lines and the flux ropes, as predicted by theoretical models (e.g., Lee et al., 1993; Lee & Fu, 1985) and confirmed by spacecraft observations and early global MHD simulations (e.g., Fuselier et al., 2018, 2019; Laitinen et al., 2007), in which the angle between the axis

10.1029/2020JA028670

of flux ropes and the equatorial plane is (180°−α)/2. In our simulations, as shown in Cases 3–5, this angle increases from 14° ($\alpha = 150°$) to 33° ($\alpha = 120°$) as the IMF clock angle decreases, which is consistent with the above dependence.

Our simulations further show that in the cases with smaller clock angles, the flux ropes are longer in the axial direction, this is because the nonzero guide field B_y makes the flux ropes more stable in the axial direction. Generally speaking, a cylindrical flux rope with radius, a, and length, $L \gg a$, is unstable to kink instability if $\ln(L/a) > |B_{0\|}|^2 / B_{0\theta}^2$ (Treumann & Baumjohann, 2001), where $B_{0\|}$ is the axial magnetic field of the flux rope and $B_{0\theta}$ is the circular magnetic field of the flux rope. In this paper, $B_{0\|} \approx B_y$, and $B_{0\theta} \approx \sqrt{B_x^2 + B_z^2}$, so the condition for kink instability of a cylindrical flux rope becomes $\ln(L/a) > |B_y|^2 / (B_x^2 + B_z^2)$. For a flux rope with a weak core field (e.g., FR_2 shown in Figures 2 and 3), its length is much larger than its radius, and its magnetic field ${B_y}^2$ is very small. For this flux rope with a weak core field, the kink instability condition is satisfied, so it can be bended due to the kink instability. For a flux rope with a strong core field (e.g., FR_2 shown in Figures 12 and 13), its magnetic field ${B_y}^2$ is very large, so this flux rope with a strong core field is stable to the kink instability and thus cannot be bended. That is, to say, if the flux ropes' axial length is much larger than its radius, and there is almost no core field within the flux rope, then kink instability (Lapenta et al., 2006; Zhu & Winglee, 1996) may be triggered more easily, which causes the bending of flux rope in its axial direction (see Figure 3c). The presence of a nonzero guide magnetic field B_y creates a strong core field in the axial direction of the flux rope, and the core field can cause large magnetic tension force to prevent the flux rope from continuing bending. In addition, the presence of a nonzero guide magnetic field B_y also facilitates the concatenation of isolated flux ropes, thus making the flux ropes longer and more stable.

Our simulations show that the magnetopause flux ropes are mostly formed near the subsolar point. If the IMF is mostly southward, in Cases 1 and 2, the flux ropes stay at the equatorial for a longer time before they move poleward, and as a result, the flux ropes can also coalesce at the equatorial plane in these two cases. However, if the IMF has a smaller clock angle, in Case 3, the flux ropes stay at the equatorial plane for a shorter time and then quick move poleward, and therefore, the coalescence between the flux ropes does not occur at the subsolar point but in a higher latitude when the flux ropes move poleward. The reason for the difference is that in Cases 1 and 2, there are strong local ion flows caused by reconnection outflows from multiple X lines near the subsolar point which allow the flux ropes to stay in the middle of the local flow patterns a long time. However, in Case 3, inefficient reconnection results in weaker local ion flows, which is overwhelmed by the background magnetosheath plasma flows, therefore, the flux ropes formed at the subsolar point are driven poleward by the background plasma flows. Similar results also occur with smaller IMF clock angle in Cases 4 and 5 ($\alpha \leq 135°$). When the clock angle further decreases, in Case 4, magnetopause reconnection can still occur to form flux ropes, but the reconnection process is less efficient because of the strong guide field B_y (e.g., Pritchett & Coroniti, 2004) and smaller reconnecting component B_z (e.g., Cassak & Shay, 2007). Therefore, the reconnection outflows are also slower, insufficient to drive flux ropes to each other to coalesce in Case 4. Regarding the formation of larger flux rope, coalescence between two flux ropes is an efficient way to form a larger flux rope (e.g., Akhavan-Tafti et al., 2018; Cazzola et al., 2015; Finn & Kaw, 1977; Hoilijoki et al., 2017). For example, FR_3 and FR_4 coalesce into a larger flux rope, $FR_{3,4}$ (see Figure 5). On the other hand, a flux rope is flanked by two reconnection X lines, therefore, continuous reconnection at the two X lines keeps feeding the flux rope with magnetic flux and plasma, which can also form a larger flux rope (Hoilijoki et al., 2019). Regarding the fate of the flux ropes, using 2-D global hybrid simulations, Omidi and Sibeck (2007) and Sibeck and Omidi (2012) have shown that the flux ropes eventually enter the cusp regions and disintegrate through a secondary magnetic reconnection process. Our simulations reveal the 3-D effects of this process and find that the flux ropes'' helical structure collapses, their core field weakens gradually, and their axial length decreases in this process.

Data Availability Statement

The data resources are from "National Space Science Data Center, National Science & Technology Infrastructure of China (http://www.nssdc.ac.cn)." The simulation results are generated from our computer simulation model, which is described in Section 2. The simulation data used to plot the figures in this study can be downloaded from https://dx.doi.org/10.12176/01.99.00147.

Acknowledgments
This research was funded by the Key Research Program of Frontier Sciences CAS (QYZDJ-SSW-DQC010), NSFC grant 4177416, 41527804, and the Strategic Priority Research Program of Chinese Academy of Sciences Grant No. XDB41000000. The authors acknowledge for the data resources from "National Space Science Data Center, National Science & Technology Infrastructure of China (http://www.nssdc.ac.cn)."

References

Akhavan-Tafti, M., Slavin, J. A., Le, G., Eastwood, J. P., Strangeway, R. J., Russell, C. T., et al. (2018). MMS examination of FTEs at the Earth's subsolar magnetopause. *Journal of Geophysical Research: Space Physics*, *123*, 1224–1241. https://doi.org/10.1002/2017JA024681

Alm, L., Farrugia, C. J., Paulson, K. W., Argall, M. R., Torbert, R. B., Burch, J. L., et al. (2018). Differing properties of two ion-scale magnetopause flux ropes. *Journal of Geophysical Research: Space Physics*, *123*, 114–131. https://doi.org/10.1002/2017JA024525

Birn, J., Borovsky, J. E., & Hesse, M. (2008). Properties of asymmetric magnetic reconnection. *Physics of Plasmas*, *15*(3), 32101. https://doi.org/10.1063/1.2888491

Cassak, P. A., & Shay, M. A. (2007). Scaling of asymmetric magnetic reconnection: General theory and collisional simulations. *Physics of Plasmas*, *14*(10), 102114. https://doi.org/10.1063/1.2795630

Cazzola, E., Innocenti, M. E., Markidis, S., Goldman, M. V., Newman, D. L., & Lapenta, G. (2015). On the electron dynamics during island coalescence in asymmetric magnetic reconnection. *Physics of Plasmas*, *22*(2015), 092901. https://doi.org/10.1063/1.4929847

Chen, Y., Tóth, G., Cassak, P., Jia, X., Gombosi, T. I., Slavin, J. A., et al. (2017). Global three-dimensional simulation of Earth's dayside reconnection using a two-way coupled magnetohydrodynamics with embedded particle-in-cell model: Initial results. *Journal of Geophysical Research: Space Physics*, *122*, 10318–10335. https://doi.org/10.1002/2017JA024186

Dorelli, J. C., & Bhattacharjee, A. (2009). On the generation and topology of flux transfer events. *Journal of Geophysical Research*, *114*, A06213. https://doi.org/10.1029/2008JA013410

Fedder, J. A., Slinker, S. P., Lyon, J. G., & Russell, C. T. (2002). Flux transfer events in global numerical simulations of the magnetosphere. *Journal of Geophysical Research*, *107*(A5), 1048. https://doi.org/10.1029/2001JA000025

Finn, J. M., & Kaw, P. K. (1977). Coalescence instability of magnetic islands. *The Physics of Fluids*, *20*(1), 72–78. https://doi.org/10.1063/1.861709

Fuselier, S. A., Petrinec, S. M., Trattner, K. J., Broll, J. M., Burch, J. L., Giles, B. L., et al. (2018). Observational evidence of large-scale multiple reconnection at the Earth's dayside magnetopause. *Journal of Geophysical Research: Space Physics*, *123*, 8407–8421. https://doi.org/10.1029/2018JA025681

Fuselier, S. A., Trattner, K. J., Petrinec, S. M., Pritchard, K. R., Burch, J. L., Cassak, P. A., et al. (2019). Stationarity of the reconnection X-line at Earth's magnetopause for southward IMF. *Journal of Geophysical Research: Space Physics*, *124*, 8524–8534. https://doi.org/10.1029/2019JA027143

Glocer, A., Dorelli, J., Toth, G., Komar, C. M., & Cassak, P. A. (2016). Separator reconnection at the magnetopause for predominantly northward and southward IMF: Techniques and results. *Journal of Geophysical Research: Space Physics*, *121*, 140–156. https://doi.org/10.1002/2015JA021417

Guo, Z., Lin, Y., Wang, X., Vines, S. K., Lee, S. H., & Chen, Y. (2020). Magnetopause reconnection as influenced by the dipole tilt under southward IMF conditions: Hybrid simulation and MMS observation. *Journal of Geophysical Research: Space Physics*, *125*. https://doi.org/10.1029/2020JA027795

Hasegawa, H., Wang, J., Dunlop, M. W., Pu, Z. Y., Zhang, Q. -H., Lavraud, B., et al. (2010). Evidence for a flux transfer event generated by multiple X-line reconnection at the magnetopause. *Geophysical Research Letters*, *37*, L16101. https://doi.org/10.1029/2010GL044219

Hoilijoki, S., Ganse, U., Pfau-Kempf, Y., Cassak, P. A., Walsh, B. M., Hietala, H., et al. (2017). Reconnection rates and X line motion at the magnetopause: Global 2D-3V hybrid-Vlasov simulation results. *Journal of Geophysical Research: Space Physics*, *122*, 2877–2888. https://doi.org/10.1002/2016JA023709

Hoilijoki, S., Ganse, U., Sibeck, D. G., Cassak, P. A., Turc, L., Battarbee, M., et al. (2019). Properties of magnetic reconnection and FTEs on the dayside magnetopause with and without positive IMF B_x component during southward IMF. *Journal of Geophysical Research: Space Physics*, *124*, 4037–4048. https://doi.org/10.1029/2019JA026821

Kacem, I., Jacquey, C., Génot, V., Lavraud, B., Vernisse, Y., Marchaudon, A., et al. (2018). Magnetic reconnection at a thin current sheet separating two interlaced flux tubes at the Earth's magnetopause. *Journal of Geophysical Research: Space Physics*, *123*, 1779–1793. https://doi.org/10.1002/2017JA024537

Karimabadi, H., Krauss-Varban, D., Omidi, N., & Vu, H. X. (1999). Magnetic structure of the reconnection layer and core field generation in plasmoids. *Journal of Geophysical Research*, *104*(A6), 12313–12326. https://doi.org/10.1029/1999JA900089

Karimabadi, H., Vu, H. X., Krauss-Varban, D., & Omelchenko, Y. (2006). Global hybrid simulations of the Earth's magnetosphere. Numerical modeling of Space plasma flows, (Vol. 359, p. 257). Astronomical Society of the Pacific.

Laitinen, T. V., Palmroth, M., Pulkkinen, T. I., Janhunen, P., & Koskinen, H. E. J. (2007). Continuous reconnection line and pressure-dependent energy conversion on the magnetopause in a global MHD model. *Journal of Geophysical Research*, *112*, A11201. https://doi.org/10.1029/2007JA012352

Lapenta, G., Furno, I., Intrator, T., & Delzanno, G. L. (2006). Kink instability of flux ropes anchored at one end and free at the other. *Journal of Geophysical Research*, *111*, A12S06. https://doi.org/10.1029/2006JA011932

Lee, L. C., & Fu, Z. F. (1985). A theory of magnetic flux transfer at the Earth's magnetopause. *Geophysical Research Letters*, *12*, 105–108. https://doi.org/10.1029/GL012i002p00105

Lee, L. C., Ma, Z. W., Fu, Z. F., & Otto, A. (1993). Topology of magnetic flux ropes and formation of fossil flux transfer events and boundary layer plasmas. *Journal of Geophysical Research*, *98*(A3), 3943–3951. https://doi.org/10.1029/92JA02203

Lin, Y., & Wang, X. (2005). Three-dimensional global hybrid simulation of dayside dynamics associated with the quasi-parallel bow shock. *Journal of Geophysical Research*, *110*, A12216. https://doi.org/10.1029/2005JA011243

Lin, Y., Wang, X. Y., Lu, S., Perez, J. D., & Lu, Q. (2014). Investigation of storm time magnetotail and ion injection using three-dimensional global hybrid simulation. *Journal of Geophysical Research: Space Physics*, *119*, 7413–7432. https://doi.org/10.1002/2014JA020005

Lu, S., Angelopoulos, V., Artemyev, A. V., Pritchett, P. L., Sun, W. J., & Slavin, J. A. (2020). Particle-in-cell simulations of secondary magnetic islands: Ion-scale flux ropes and plasmoids. *The Astrophysical Journal*, *900*, 145. https://doi.org/10.3847/1538-4357/abaa44

Øieroset, M., Phan, T. D., Haggerty, C., Shay, M. A., Eastwood, J. P., Gershman, D. J., et al. (2016). MMS observations of large guide field symmetric reconnection between colliding reconnection jets at the center of a magnetic flux rope at the magnetopause. *Geophysical Research Letters*, *43*, 5536–5544. https://doi.org/10.1002/2016GL069166

Oka, M., Phan, T.-D., Krucker, S., Fujimoto, M., & Shinohara, I. (2010). Electron acceleration by multi-island coalescence. *The Astrophysical Journal*, *714*, 915–926. http://doi.org/10.1088/0004-637X/714/1/915

Omidi, N., Blanco-Cano, X., Russell, C. T., & Karimabadi, H. (2004). Dipolar magnetospheres and their characterization as a function of magnetic moment. *Advances in Space Research*, *33*, 1996–2003. https://doi.org/10.1016/j.asr.2003.08.041

Omidi, N., & Sibeck, D. G. (2007). Flux transfer events in the cusp. *Geophysical Research Letters*, *34*, L04106. https://doi.org/10.1029/2006GL028698

Paschmann, G., Haerendel, G., Papamastorakis, I., Sckopke, N., Bame, S. J., Gosling, J. T., & Russell, C. T. (1982). Plasma and magnetic field characteristics of magnetic flux transfer events. *Journal of Geophysical Research*, *87*(A4), 2159–2168. https://doi.org/10.1029/JA087iA04p02159

Phan, T. D., Hasegawa, H., Fujimoto, M., Oieroset, M., Mukai, T., Lin, R. P., & Paterson, W. R. (2006). Simultaneous Geotail and Wind observations of reconnection at the subsolar and tail flank magnetopause. *Geophysical Research Letters*, *33*, L09104. https://doi.org/10.1029/2006GL025756

Pritchett, P. L. (2001). Geospace Environment Modeling magnetic reconnection challenge: Simulations with a full particle electromagnetic code. *Journal of Geophysical Research*, *106*(A3), 3783–3798. https://doi.org/10.1029/1999JA001006

Pritchett, P. L. (2008). Energetic electron acceleration during multi-island coalescence. *Physics of Plasmas*, *15*, 102105. http://doi.org/10.1063/1.2996321

Pritchett, P. L., & Coroniti, F. V. (2004). Three-dimensional collisionless magnetic reconnection in the presence of a guide field. *Journal of Geophysical Research*, *109*, A01220. https://doi.org/10.1029/2003JA009999

Raeder, J. (2006). Flux transfer events: 1. Generation mechanism for strong southward IMF. *Annales Geophysicae*, *24*(1), 381–392. https://doi.org/10.5194/angeo-24-381-2006

Russell, C. T., & Elphic, R. C. (1978). Initial ISEE magnetometer results: magnetopause observations. *Space Science Reviews*, *22*, 681–715. https://doi.org/10.1007/BF00212619

Sibeck, D. G., & Omidi, N. (2012). Flux transfer events: Motion and signatures. *Journal of Atmospheric and Solar: Terrestrial Physics*, *87*, 20–24. https://doi.org/10.1016/j.jastp.2011.07.010

Swift, D. W. (1996). Use of a hybrid code for global-scale plasma simulation. *Journal of Computational Physics*, *126*(1), 109–121. https://doi.org/10.1006/jcph.1996.0124

Tan, B., Lin, Y., Perez, J. D., & Wang, X. Y. (2011). Global-scale hybrid simulation of dayside magnetic reconnection under southward IMF: Structure and evolution of reconnection. *Journal of Geophysical Research*, *116*, A02206. https://doi.org/10.1029/2010JA015580

Tóth, G., Chen, Y., Gombosi, T. I., Cassak, P., Markidis, S., & Peng, I. B. (2017). Scaling the ion inertial length and its implications for modeling reconnection in global simulations. *Journal of Geophysical Research: Space Physics*, *122*, 10336–10355. https://doi.org/10.1002/2017JA024189

Tóth, G., Jia, X., Markidis, S., Peng, I. B., Chen, Y., Daldorff, L. K. S., et al. (2016). Extended magnetohydrodynamics with embedded particle-in-cell simulation of Ganymede's magnetosphere. *Journal of Geophysical Research: Space Physics*, *121*, 1273–1293. https://doi.org/10.1002/2015JA021997

Treumann, R. A., & Baumjohann, W. (2001). *Advanced space plasma physics*, (pp. 64–65). London: Imperial College Press.

Wang, H. Y., Lu, Q. M., Huang, C., & Wang, S. (2016b). The mechanisms of electron acceleration during multiple X line magnetic reconnection with a guide field. *The Astrophysical Journal*, *821*, 84. http://doi.org/10.3847/0004-637X/821/2/84

Wang, R. S., Lu, Q. M., Nakamura, R., Baumjohann, W., Russell, C. T., Burch, J. L., et al. (2017). Interaction of magnetic flux ropes via magnetic reconnection observed at the magnetopause. *Journal of Geophysical Research: Space Physics*, *122*, 10436–10447. https://doi.org/10.1002/2017JA024482

Winglee, R. M., Harnett, E., Stickle, A., & Porter, J. (2008). Multiscale/multifluid simulations of flux ropes at the magnetopause within a global magnetospheric model. *Journal of Geophysical Research*, *113*, A02209. https://doi.org/10.1029/2007JA012653

Zhong, J., Pu, Z. Y., Dunlop, M. W., Bogdanova, Y. V., Wang, X. G., Xiao, C. J., et al. (2013). Three-dimensional magnetic flux rope structure formed by multiple sequential X-line reconnection at the magnetopause. *Journal of Geophysical Research*, *118*, 1904–1911. https://doi.org/10.1002/jgra.50281

Zhou, M., Berchem, J., Walker, R. J., El-Alaoui, M., Deng, X., Cazzola, E., et al. (2017). Coalescence of macroscopic flux ropes at the subsolar magnetopause: magnetospheric multiscale observations. *Physical Review Letters*, *119*, 055101. https://link.aps.org/doi/10.1103/PhysRevLett.119.055101

Zhu, Z., & Winglee, R. M. (1996). Tearing instability, flux ropes, and the kinetic current sheet kink instability in the Earth's magnetotail: A three-dimensional perspective from particle simulations. *Journal of Geophysical Research*, *101*(A3), 4885–4897. https://doi.org/10.1029/95JA03144